From the roundabout of molecular events to nanomaterial-induced chronic inflammation prediction

Authors:

Hana Majaron*, Boštjan Kokot*, Aleksandar Sebastijanović*, Carola Voss, Rok Podlipec, Patrycja Zawilska, Trine Berthing, Carolina Ballester López, Pernille Høgh Danielsen, Claudia Contini, Mikhail Ivanov, Ana Krišelj, Petra Čotar, Qiaoxia Zhou, Jessica Ponti, Vadim Zhernovkov, Matthew Schneemilch, Zahra Manel Doumandji, Mojca Pušnik, Polona Umek, Stane Pajk, Olivier Joubert, Otmar Schmid, Iztok Urbančič, Martin Irmler, Johannes Beckers, Vladimir Lobaskin, Sabina Halappanavar, Nick Quirke, Alexander Lyubartsev, Ulla Vogel, Tilen Koklič**, Tobias Stoeger**, Janez Štrancar**

Abstract

Many chronic diseases manifest in prolonged inflammation and often ignored dysregulated lipid metabolism. When associated with inhalation of nanomaterials, limited information is available on the relevant molecular events and their causal connections. This prevents reliable prediction of outcomes by efficient testing strategies. To unravel how acute nanomaterial exposure leads to chronic conditions, we employed advanced microscopy and omics *in vitro* and *in vivo* together with *in silico* modelling. For selected metal-oxide nanomaterials, we show that lung epithelial cells survive the exposure by excreting internalized nanomaterials and passivating them on the surface, employing elevated lipid synthesis. Macrophages, on the contrary, lose their integrity whilst degrading the passivized bio-nano agglomerates, releasing the nanomaterials, which are taken up again by the epithelial cells. Constant proinflammatory signalling recruits new phagocytes that feed the vicious cycle of events, resulting in a long-lasting response to a single exposure. The proposed mechanism explains the nanomaterial-associated *in vivo* chronic outcomes and allows its prediction based on *in vitro* measurements. Similar mechanisms may trigger other chronic diseases affecting millions of lives worldwide.

Introduction - Mechanism of persistent inflammation unknown

Today, chronic diseases such as asthma, lung cancer, heart disease, and brain damage with accelerated cognitive decline, are considered to be some of the most significant causes of death [1–3]. These diseases are known to be associated with air pollution and inhalation of particulate matter and nanoparticles [4], which, according to the OECD and WHO, kill four million people globally every year [5,6]. Therefore, the ever-increasing production of nanomaterials, as consequence of the rapidly developing and extremely promising nanotechnology industry, generates concerns about potential human exposure and health impacts. Due to the lack of understanding of how these adverse outcomes evolve, decision-makers around the world (OECD, US EPA, NIH, EC, JRC, etc.) recognized the need to elucidate the molecular mechanisms involved in adverse outcome pathways (AOPs) [7]. The latter have emerged as the most promising construct in creating predictive toxicology, capable of forecasting the apical endpoints based on the detection of the key events of toxicity pathways using *in vitro* tests as inexpensive and high-throughput alternative testing strategies [8].

Despite some advances in the development of targeted test assays [9] and QSAR [10] models for nanotoxicology, currently neither *in vitro* nor *in silico* tools are able to reliably predict *in vivo* adverse outcomes [11,12]. The task is especially challenging in regard of systemic and chronic adverse effects, which are associated with pathological changes that evolve in organs and tissues over long time. *In vitro* systems are often incapable of exhibiting the *in vivo* mechanism of action of the nanomaterial and reproducing the long-term processes *in vivo.* Combined with the lack of understanding of underlying mechanisms and the associated molecular events behind the adverse outcome pathways, prediction of chronic outcomes is currently completely precluded.

Exceptionally long-lasting inflammatory responses, reflected in prolonged accumulation of infiltrated leukocytes in the lungs, have been shown to follow both single [13–18] and repetitive exposure [19–21] to some nanomaterials. The insolubility and bio-persistency of the particles have been associated with continuous release of pro-inflammatory mediators from irritated resident cells or dying immune cells, frequently co-observed with chronic dysregulated lipid metabolism [22–27].

Here we show on selected nanomaterials that both chronically dysregulated lipid metabolism and chronic inflammation originate from nanomaterial cycling between a passivated lipid-wrapped form on epithelial cells and an uncoated bare form released from dying phagocytes. The mechanistic picture of the lifecycle and understanding of the mechanism of action of the nanomaterial led us to design a conceptually novel testing strategy employing a minimal combination of *in vitro* and *in silico* tests to classify nanomaterials with respect to the predicted *in vivo* outcome.

Results and discussion
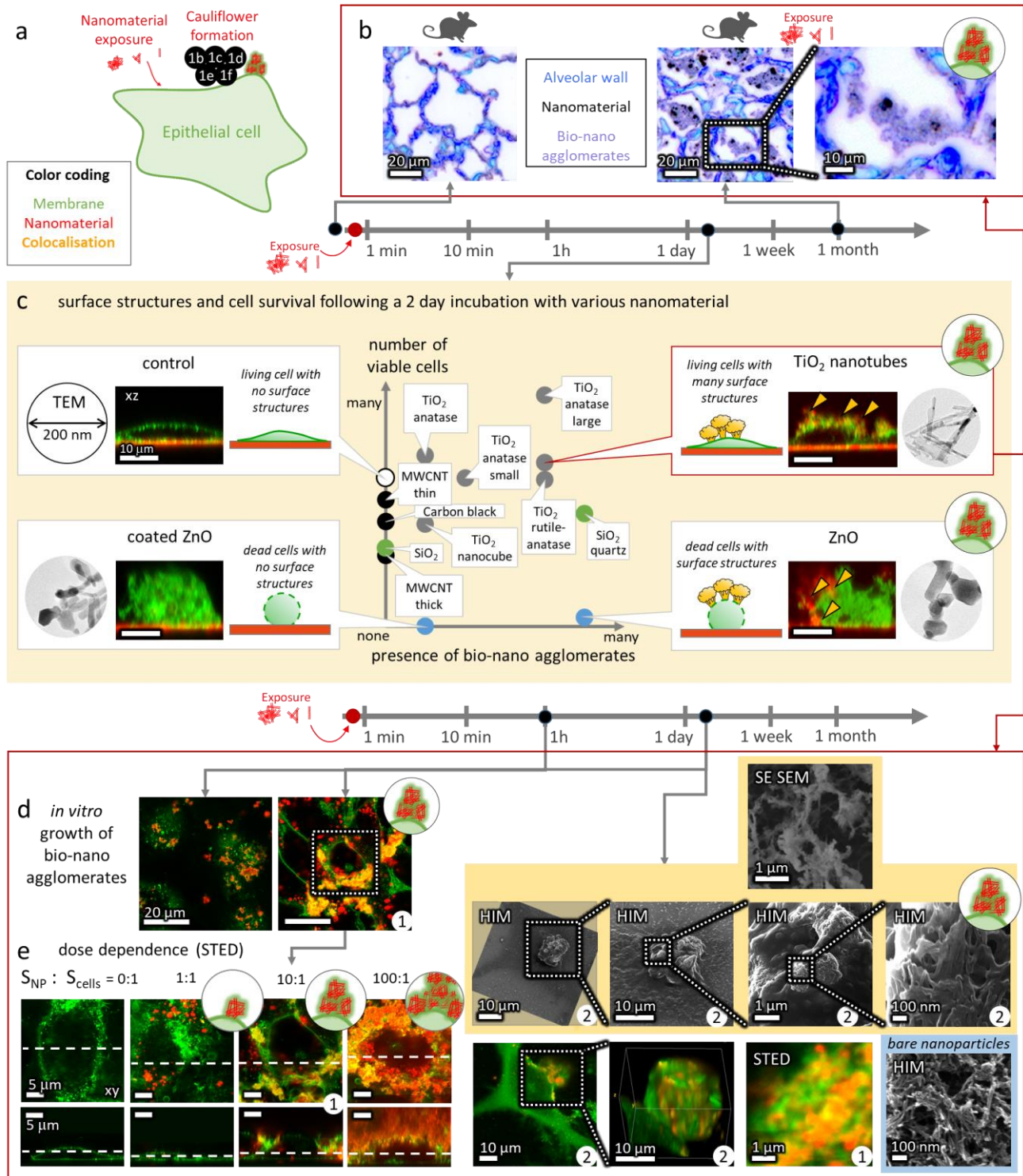
1. Passivation of nanomaterials

Fig. 1: Formation of bio-nano agglomerates on epithelial cell surface, referred to as cauliflowers. *a* A general scheme of events shown in this figure. *b* Hyperspectral-colour-inverted darkfield micrographs of TiO₂ nanotubes (black) in bio-nano agglomerates (violet) observed in alveoli (blue) 1 month after instillation of the

*nanomaterial in mice. In fluorescence micrographs of in vitro alveolar epithelial (LA-4) cells **c-f** membranes are shown in green and nanoparticles in red. Images with the same number in the lower right corner are images of the same cell. **c** Presence of cauliflowers, cell survival and xz cross-sections after a 2-day exposure to several nanomaterials at nanomaterial-to-cell surface ratio ($S_{NP}:S_{cells}$) of 10:1 (nanoparticles observed in backscatter). Inserts show 200 nm-large TEM micrographs of nanoparticles used. **d** Time-dependent cauliflower formation by LA-4 exposed to TiO_2 nanotubes at $S_{NP}:S_{cells} = 10:1$. **e** Super-resolved STED xy and xz cross-sections of dose-dependent cauliflower growth reveal that cauliflowers are located on the outer surface of cells after 2 days. $S_{NP}:S_{cells}$ are 0:1, 1:1, 10:1 and 100:1. **f** link to 3D: ▱ High-resolution correlative STED, SE SEM and HIM images reveal the detailed structures of cauliflowers at a $S_{NP}:S_{cells} = 10:1$. For associated data see chapter S1in Supplementary Information (SI).*

To uncover the causal relationships between events leading from pulmonary nanomaterial exposure to chronic inflammation, we applied a complex set of complementary *in vivo*, *in vitro* and *in silico* experiments employing state-of-the-art microscopy, spectroscopy, omics and modelling approaches. TiO_2 nanotubes were selected as the model material because they induce very high and long-lasting chronic inflammatory responses *in vivo* accompanied by markedly disturbed alveolar integrity of the lungs, defined as alveolar proteinosis [13], with bio-nano agglomerates in the alveoli (Fig. 1b, violet structures). Importantly, this nanomaterial induces similar bio-nano agglomerate structures on the surface of the lung epithelial cells *in vitro* (Fig. 1c). With cells remaining viable for longer period after exposure, this *in vitro* system allows us to study the detailed mechanism of the inflammatory response. Note, that similar structures were observed both *in vivo* and *in vitro* after exposure to crystalline quartz (DQ12), a well-known occupational hazard causing pulmonary alveolar proteinosis (PAP) [13], but not for all carbon nanotubes (CNTs)[27,28].

We have previously observed that TiO_2 nanotubes can wrap themselves in the constituents of epithelial plasma membranes and relocate these molecules efficiently across the epithelial layer [29] at a low concentration of nanotubes (surface-of-nanomaterial-to-cell-surface dose 1:1) due to their high affinity for lipids. Thus, it is expected that at higher surface doses, these nanoparticles should completely disrupt the epithelial cell membranes. Surprisingly, our current experiments show that the epithelial cells survive exposures to surface doses as high as 100:1 (Fig. 1e, Supplementary Information (SI) sections S0e and S0f). A few days after exposure, the majority of the nanoparticles are found in large bio-nano agglomerates on the epithelial surface, consisting of at least nanoparticles and lipids, which we term cauliflowers due to their shape in our fluorescence micrographs (Fig. 1d, Fig. 1e, yellow colour).

Because cauliflowers are observed exclusively on the surface of epithelial cells, not inside (Fig. 1e, Fig. 1f), the formation of cauliflowers might be driven solely by physical interactions between nanoparticles and lipids as in the case of lipid wrapping. However, excessive amount of lipids colocalized with nanoparticles in the cauliflower structures two days after the exposure suggests an involvement of active biological response, e.g. increased lipid production, explored next.
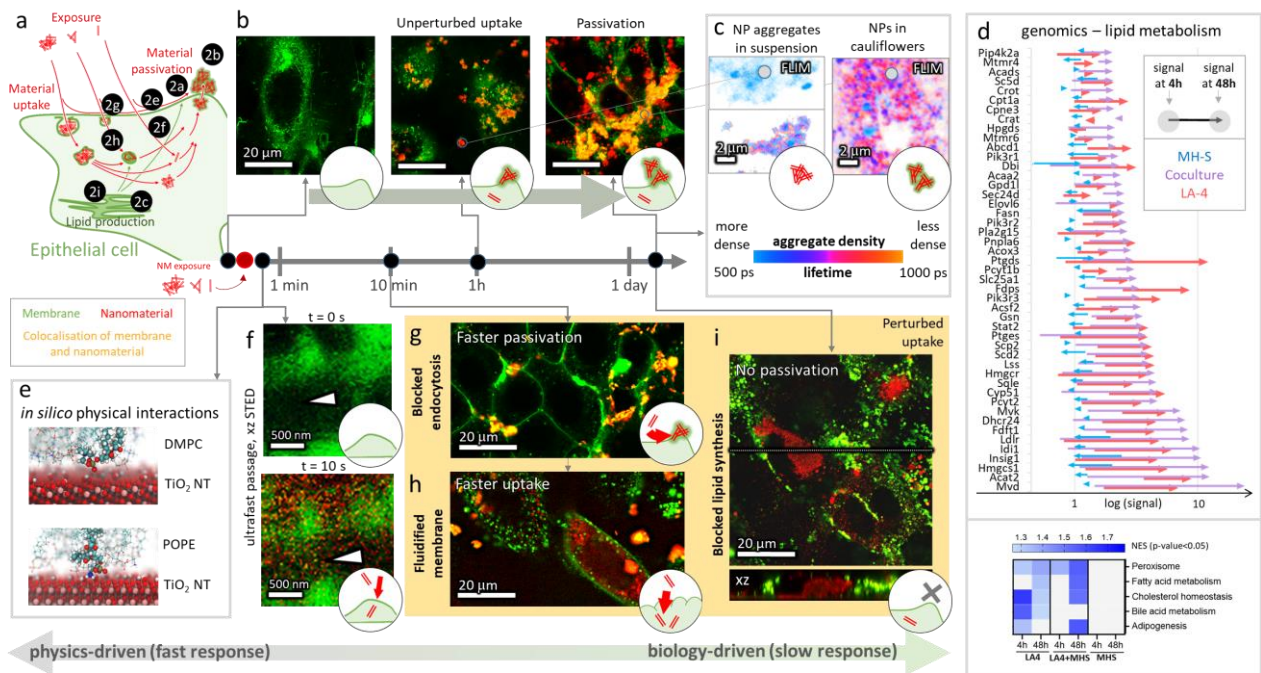
2. The role of lipids

Fig. 2: Role of lipids in cauliflower formation. a *General scheme of events. In fluorescence micrographs in vitro, cell membranes are displayed in green and TiO$_2$ nanotubes in red, surface dose was 10:1 (except **f**). **b** Unperturbed uptake of TiO$_2$ nanotubes after 0, 1 h and 2 days by lung epithelial LA-4 cells, same as Fig. 1d. **c** Increased fluorescence lifetime (FLIM) of fluorophore on TiO$_2$ nanotubes in cauliflowers (right) compared to agglomerates in suspension (left) corresponds to increased distance between fluorophores on the nanotubes (e.g. separation due to lipid interspacing). **d** Transcriptional signature of lipid metabolism genes (top) and hallmark gene sets(bottom) for MH-S macrophages (blue), LA-4 epithelial cells(red) and their co-culture (purple) after 4 hours (beginning of arrow) and 48 hours (end of arrow) of nanomaterial exposure (NES). **e** Final state of full-atom in silico simulation confirms strong interaction between disordered lipids and the TiO$_2$ nanotubes (DMPC links to movie and 3D: 🎥 🗔, POPE 🎥 🗔). **f** 🎥 xz cross-sections immediately before (above) and 10 s after (below) instant delivery of TiO$_2$ nanotubes onto cells by nebulisation (1:1 surface dose) show ultrafast membrane passage of the nanotubes through the cell plasma membrane into the cell (arrowhead). Drug-perturbed uptakes (to compare with **b**): **g** 🎥 🗔 chlorpromazine-blocked clathrin-mediated endocytosis,*

h ☐ *fluidified cell plasma membrane induced by cholesterol depletion (beta-methyl-cyclodextrin)* *i* ☐ *inhibited fatty acid synthesis (resveratrol-blocked fatty-acid synthase). For associated data see SI chapter S2.*

Coinciding with the formation of the lipid-rich bio-nano agglomerates (Fig. 2b), i.e. two days after the nanomaterial exposure, a strong upregulation of membrane lipid metabolism-related genes is observed (Fig. 2d). Further modulation of the lipid synthesis pathway by blocking its key enzyme, fatty acid synthase (FAS), with resveratrol precludes the formation of large cauliflowers (Fig. 2i), confirming that epithelial cells respond to nanomaterial exposure by an increased lipid synthesis, which is in turn required for cauliflower formation.

As internalization of nanoparticles typically precedes cauliflower formation, we investigate the causal relationship between the two phenomena by blocking an important route of nanoparticle uptake, i.e. clathrin-mediated endocytosis (SI section S0d), using chlorpromazine. Interestingly, small "proto" cauliflowers are formed soon after exposure (15 min time scale) (Fig. 2g), indicating an additional mechanism of formation that requires no intracellular processing. In this case, formation of cauliflowers presumably relies on the strong physical affinity between nanoparticles and lipids, also supported by *in silico* simulations (Fig. 2e) and *in vitro* experiments on model lipid membranes (SI section S0c). However, these "proto" cauliflowers are rarely seen under normal conditions, which lead us to conclude that this additional mechanism of formation is usually less likely, possibly due to the efficient particle uptake that displaces nanomaterial away from the plasma membrane, preventing their further interaction.

Under unperturbed exposure (Fig. 2b), a direct physical interaction between nanoparticles and membrane lipids might therefore lead to their agglomeration and thus initiate the formation of cauliflowers anchored to the membrane. The depletion of the functional lipids may trigger additional lipid synthesis, which later enables passivation of even higher doses of nanoparticles in large agglomerates on the cellular surface (Fig. 1e). It is noteworthy that nanoparticles in these cauliflowers are effectively dispersed by interspaced lipids and therby more loosely packed compared to agglomerates of pure nanoparticles, as seen by increased fluorescence lifetime (Fig. 2c).

Interestingly, depletion of cholesterol as the major membrane constituent by beta-methyl-cyclodextrin, which increases the fluidity of the plasma membrane, leads to strong suppression of fast (membrane-lipid-drain only) cauliflower formation (Fig. 2h). This indicates an important interaction between nanoparticles and cholesterol, which is reflected in strongly upregulated cholesterol and lipid synthesis pathways in epithelial cells *in vitro* (Fig. 2d heatmap, SI section S2d), as well as in mouse lungs *in vivo* (SI section S2d) [26,30,31]. In the case of cholesterol-depleted plasma membranes, the majority of

nanoparticles cross the plasma membranes on a timescale of minutes, resulting in a fine distribution of particles inside the cell. The dominant role of such a passage can also be observed when nanoparticles are delivered in a highly dispersed form through an aerosol directly to the epithelial plasma cell membranes and pass through them in a matter of seconds (Fig. 2f, link to movie: 🎥).

Particularly for the alveolar barrier of the lung, the lipid-synthesis-driven formation of bio-nano agglomerates thus seems to be an important part of an active response of alveolar epithelial cells, enabling their survival after exposure to nanomaterial even at higher doses. Thus, this process can be seen as passivation of the nanomaterial, and as a kind of protective mechanism (SI sections S0e and S0g). As we consistently observed passivized nanomaterials on the cell surface, we further explore the cellular mechanisms that facilitate the export of the internalised material.
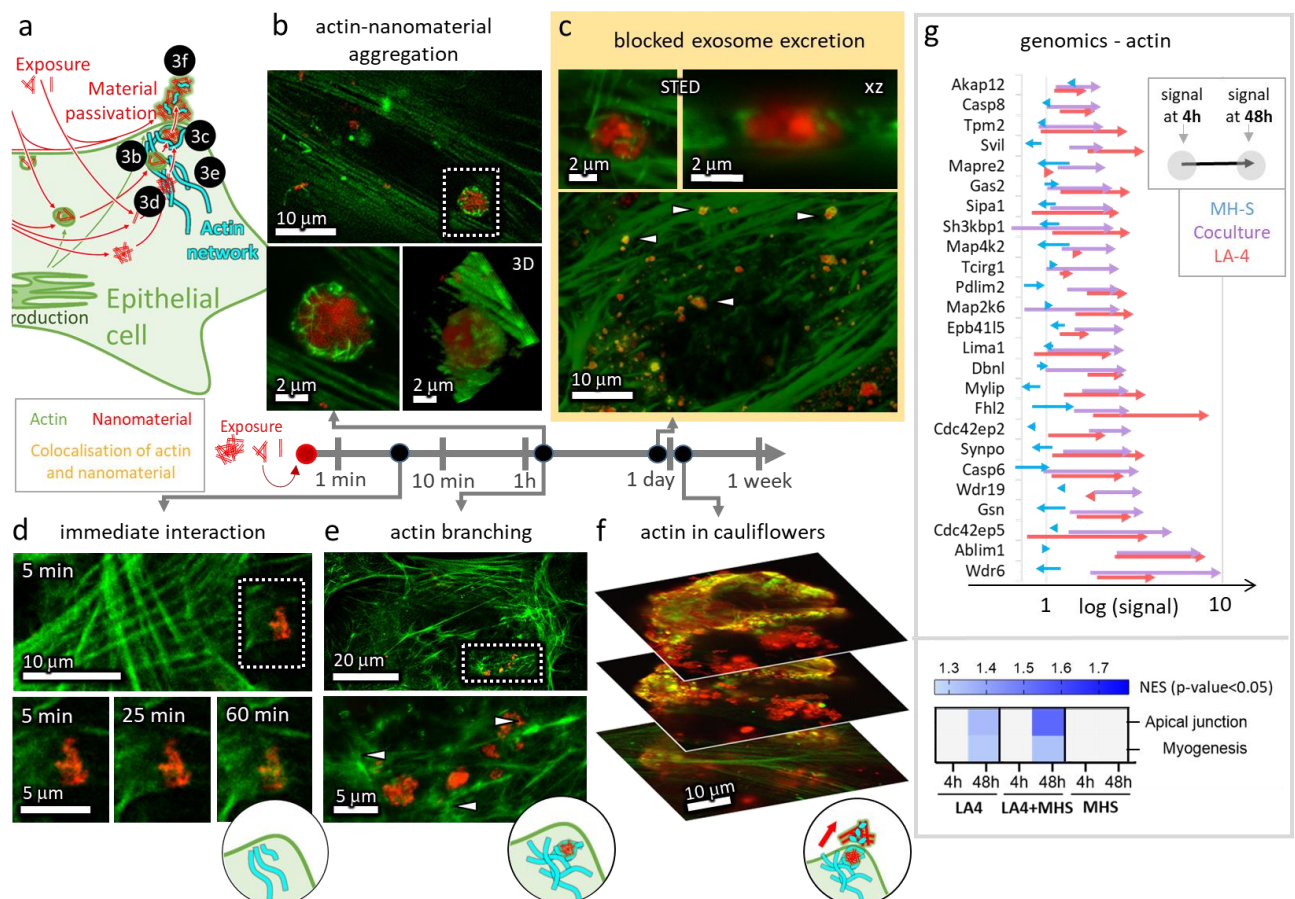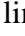
3. The role of actin

***Fig. 3: Role of actin in cauliflower formation. a** General scheme of events. Fluorescence micrographs of the actin network of LA-4 cells (green) after exposure to TiO₂ nanotubes (red) at a 10:1 surface dose. **d** 🎥 Soon after exposure, actin interacts with internalized nanoparticles, **b** 🔲 leading to formation of actin-nanoparticle agglomerates after a few hours. **e** Synchronously, the actin network branches (arrowheads), indicating changes*

in internal processes and reshaping of the cell. **c** ☐ *Blocking the final stage of exocytosis with jasplakinolide traps nanoparticles in actin rings, prepared for exocytosis (arrowheads and zoom-ins).* **f** ☐ *After a few days, actin fragments are observed in cauliflowers (arrowheads).* **g** *Transcriptional signature of actin-network related genes (top) and hallmark gene sets (bottom) for LA-4 (red), macrophages (blue), and their co-cultures (purple) after 4 hours (beginning of arrow) and 48 hours (end of arrow) of nanomaterial exposure. For associated data see SI chapter S3.*

As exocytosis involves cytoskeletal actin remodelling, we examined the role of actin in the process. Almost simultaneously with nanoparticle uptake and far before cauliflowers form, many nanoparticles interact with actin fibres (Fig. 3d), forming nanoparticle-actin 3D agglomerates resembling Faberge eggs (Fig. 3b). Hours after exposure, the same interaction causes actin network transformations from linear aligned to branched fibres (Fig. 3e), which is associated with increased cell motility [32] as well as with internal vesicular trafficking [33,34] and nanoparticle exocytosis [35,36].

By blocking actin fibre dynamics (polymerization and depolymerisation) with jasplakinolide, excretion of exocytotic vesicles can be stopped, thereby enabling their simultaneous visualisation and identification. Namely, after uptake of nanoparticles and lipid synthesis, nanoparticles are trapped in exocytotic vesicles (actin rings), prepared for exocytosis by the cell (Fig. 3c). As actin can be identified extracellularly within cauliflowers (Fig. 3f, link to 3D: ☐), excretion of nanoparticles is apparently more destructive to the actin network than normal, homeostatic exocytosis, where actin is retained inside cells. Actin adherence is also reflected in the coronome analysis of the mobile fraction of nanoparticles after exposure, in which we have previously detected an abundant fraction of actin proteins [29]. This clearly coincides with the upregulation of pathways related to actin synthesis (Fig. 3g). Until now, the appearance of actin in the nanoparticle corona outside of the cells could not be explained.

The creation of cauliflowers on the cell surface thus involves both membrane lipids and actin (heatmaps in Fig. 2d and Fig. 3c) that directly interact with the nanoparticle surface. Due to the strong binding of amines and phosphates identified by *in silico* simulations (Fig. 2e) it is reasonable to expect that biomolecules, including lipids, proteins and nucleic acids, strongly bind to the same particle surface. Moreover, multiple binding sites on the nanomaterial and biomolecules or their supramolecular structures directly lead to crosslinking and formation of large bio-nano agglomerates, such as the observed cauliflowers. This implies that any strong interaction reflected in noticeable binding within identified within *in silico* modelling of biomolecule-nanomaterial surface pairs, is highly predictive of bio-nano agglomerates formation.

The ability of the alveolar epithelium to supply enough biomolecules to crosslink and thereby passivate the received dose of nanomaterial explains their survival even at relatively large local doses of nanomaterials, which can be observed also *in vivo* (Fig. 1). The process of passivation, however, seems to contradict the observation of simultaneous chronic pulmonary inflammation, raising the question about the role of neighbouring cells, especially the alveolar macrophages, which are responsible for the alveolar immune defence and thereby alveolar integrity. To address this, we expose a co-culture of LA-4 epithelial cells and MH-S alveolar macrophages in the same way as we did with the epithelial monoculture.
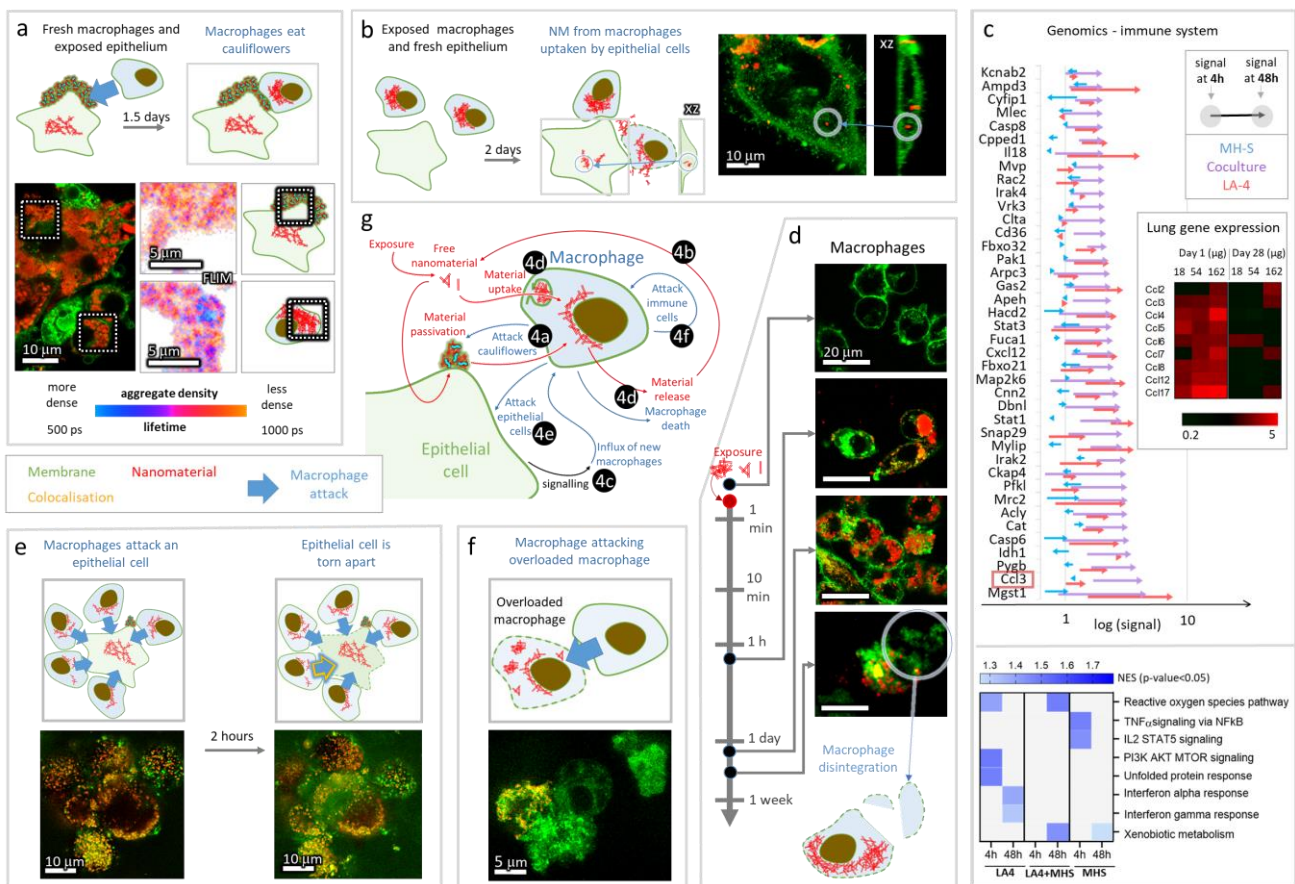
4. Macrophage action against epithelial defence
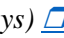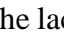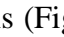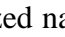
Fig. 4: The cycle of uptake, passivation and release in nanomaterial-exposed co-culture. *In all fluorescence micrographs, cell membranes are displayed in green and TiO$_2$ nanotubes in red, and the surface dose of nanoparticles is 10:1.* ***a*** *Unexposed macrophages (MH-S) were added to washed LA-4 cells with cauliflowers. Within 1.5 days, MH-S phagocyte the cauliflowers from the LA-4 cell surface, and degrade their organic (lipid) part, thereby compacting the nanoparticle agglomerates (fluorescence-lifetime-maps FLIM, right).* ***b*** *Washed nanomaterial-laden MH-S were added to unexposed LA-4. After 2 days, the nanomaterial is found in LA-4 cells*

*(encircled). **c** Transcriptional signature of genes related to the immune response (top) and hallmark gene sets (bottom) for LA-4 (red), MH-S (blue) and their co-culture (purple) after 4 hours (beginning of arrow) and 48 hours (end of arrow) of nanomaterial exposure, with lung gene expression of some CCL monocyte attractants after 1 and 28 days. **d** Nanoparticle uptake by MH-S followed by their disintegration after a few days (encircled): ☐ 🐭 (control) ☐ 🐭 (2 h) ☐ 🐭 (2 days) ☐ (4 days, MH-S disintegration) **e** 🐭 Time-lapse of MH-S attacking and tearing apart a nanomaterial-laden LA-4 cell. **f** ☐ MH-S observed attacking another nanomaterial-laden macrophage. **g** A general scheme of events shown in this figure. For associated data see SI chapterS4.*

With a co-culture of MH-S alveolar macrophages on top of nearly confluent LA-4 epithelial cells we aimed to mimic the cell populations of the alveolar surface, where alveolar macrophages represent approximately 3-5% of all the alveolar cells[37]. Upon exposure of the co-culture to TiO_2 nanotubes, part of the material gets internalized by the phagocytes, which cannot entirely prevent nanomaterial from reaching epithelial cells (SI section S0h 🐭), and is in line with previous studies [38]. Aside from that, macrophages slow down considerably after having taken up large amounts of nanoparticles (graph in SI section S0h), making their clearance function even less efficient. We note that the exposed epithelium also produces cauliflowers in our co-culture (SI section S0h), reproducing the bio-nano agglomerates observed *in vivo* in the alveolar region of the lungs of particle exposed mice (Fig. 1b) [13].

Although the nanoparticles are passivated in cauliflowers on the surface of LA-4 cells, enabling their survival, the same structures trigger the attack of macrophages, as seen in the experiment when unexposed macrophages were added to pre-exposed and therefore cauliflower-rich epithelium (Fig. 4a). After internalisation of the agglomerates, macrophages are able to degrade only their organic part as revealed by the decreased lifetime of fluorescent probes bound to the nanoparticles, indicating denser packing of nanoparticles in macrophages compared to cauliflowers (FLIM maps in Fig. 4a insets). Unwrapping the passivated nanoparticles exposes the macrophage interior to bare nanoparticles' surface, leading to the macrophage death and subsequent disintegration as observed in monoculture (Fig. 4d ☐), possibly caused by the lack of exocytosis and supressed (normally) elevated lipid synthesis signature (Fig. 2c). A similar fate is observed also after macrophages have attacked epithelial cells (Fig. 4e 🐭) or other macrophages with internalized nanomaterials (Fig. 4f ☐). When nanomaterial-exposed macrophages die, they release bare nanomaterial, which is later taken up again by epithelial cells. This can be observed experimentally: after nanomaterial-laden macrophages were added to the unexposed epithelial layer, nanoparticles are localized inside epithelial cells (Fig. 4b).

This reuptake in turn, again leads to passivated nanomaterial on the self-protected epithelial cells. *In vivo* however, dead macrophages are replaced through an influx of new monocyte-derived macrophages, attracted to the site by respective macrophage/monocyte chemoattractants such as C-C

motif ligand 3 (Ccl3)) from epithelial cells, or Ccl2-17 for the lungs of nanomaterial exposed mice (SI section S2d) [26]. This macrophage replenishment brings the entire system to conditions very similar to the initial exposure, while the reuptake of nanomaterial by the epithelium finally closes the chain of events, together forming a vicious cycle generating a never before seen loop of persistent inflammation (Fig. 4g, Fig. 5a).

Strikingly, the same chemokine expressions can be detected both *in vivo* (Fig. 4c inset) and *in vitro* in the co-culture of LA-4 and MH-S cells (Fig. 4c, purple arrows), but not in the monocultures of LA-4 (Fig. 4c, red arrows) nor in MH-S (Fig. 4c, blue arrows). This proinflammatory signalling represents the last missing piece of evidence that the *in vitro* co-culture can reproduce the entire cycle of the chronic inflammation initiating mechanism (black arrow in Fig. 4g). Can we thus predict such an *in vivo* chronic inflammation response by measuring specific states of simple *in vitro* tests?

5. Acute or chronic? The birth of predictive tools
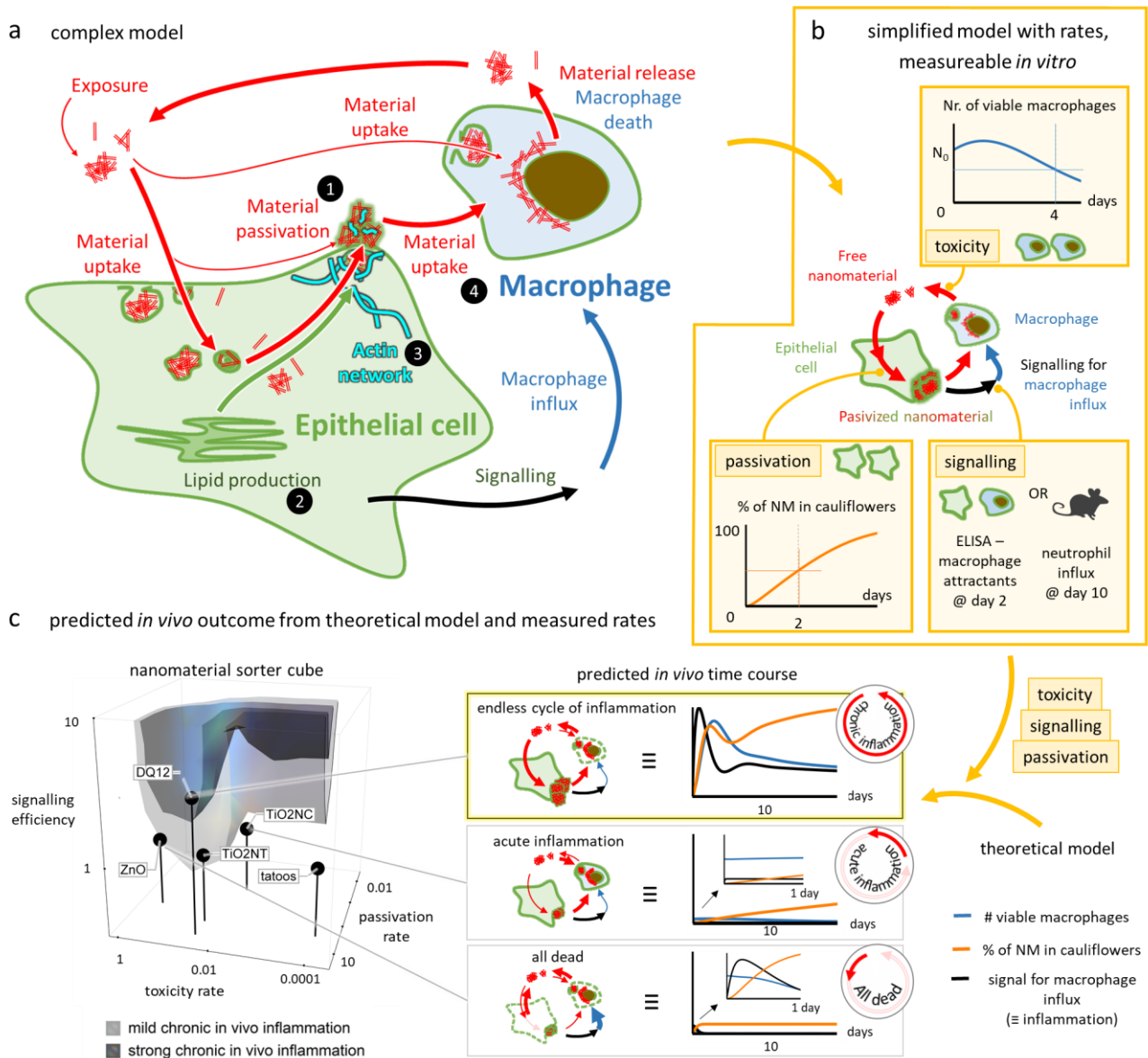
Fig. 5: Cycle of uptake, passivation and release of nanomaterial between epithelial cells and macrophages in co-cultures. a *The grand scheme connecting all inter- and intracellular events from Figures 1 − 4, simplified to **b** theoretical model, defined by rates of cauliflower formation, nanomaterial toxicity and signalling efficiency. These nanomaterial descriptors can be determined from single time-point measurements in vitro and/or in vivo. **c** The model is evaluated using these determined parameters, producing in vivo time courses (right) of the relative amount of nanomaterial in cauliflowers (orange), the number of viable macrophages (blue) and the signal for their influx (black). The value of the latter at day 10, when the acute phase is expected to subside, is contoured in the 3D space of the afore-mentioned rates (cube on the left). Nanomaterials are placed in the same 3D cube according to their measured descriptors, enabling the prediction of the degree of nanoparticle-induced chronic inflammation. For associated data see SI chapterS5.*

The proposed pathway (Fig. 5a) connecting an acute nanoparticle exposure to the chronic inflammation via a chain of causally-related events allows us to construct a simplified cyclical theoretical model, which describes the nanomaterial flow between four distinguished compartments (outside the cells, inside epithelial cells, passivated in cauliflowers, and in macrophages). This model is defined with three key descriptors (SI section S5b, depicted in Fig. 5b), measurable in appropriate *in vitro* assays for any nanomaterial of interest (yellow shaded boxes in Fig. 5b):

1) The rate of toxicity of the nanomaterials to individual cells *(tox)* is determined via the measured number of viable macrophages in MH-S monoculture after 4 days (Fig. 5b, toxicity);

2) The rate of nanomaterial passivation by epithelial cells *(cff)* is calculated from the rate *tox* and the measured fraction of nanomaterial in cauliflowers in LA-4 monoculture after 2 days (Fig. 5b, passivation);

3) The efficiency of signaling and monocyte influx replacing the dying macrophages *(signalEff)* is calculated from the rates *tox, cff* and either via measured macrophage attractants in *in vitro* co-culture of LA-4 and MH-S after 2 days or via measured influx of inflammatory cells (polymorphonuclear leukocyte) *in vivo* after at least 10 days (Fig. 5b, signalling), a time point where chronification of the response is secured.

Whether the cycle stops or continues indefinitely, depends heavily on the rates of the associated processes, calculated from the measured descriptors as described in SI section S5b. Using these rates, the model can predict the *in vivo* fate of nanomaterial passivated in cauliflowers, signaling for macrophage influx, as well as of the total macrophage number, and accordingly predict the nanomaterial-specific acute-to-chronic inflammation outcome (Fig. 5c - time traces). For example, for a very toxic nanomaterial such as ZnO, the model yields a rapid decline in the number of all cells, preventing passivation as well as influx of new macrophages, resulting in destruction of the alveolar layer [39]. For a material with intermediate toxicity and passivation rate, e.g. TiO_2 nanocubes, the model predicts weak transient inflammation, with all nanomaterial ending up in cells, as observed *in vivo* [13]. Finally, for a material such as TiO_2 nanotubes or DQ12 with intermediate toxicity and high passivation rate, persistently high inflammation and large cauliflowers (Fig. 5c – time traces) are predicted, reproducing *in vivo* observations (Fig. 1b). In this 3D space of nanomaterial descriptors (Fig. 5c – 3D plot), we can now delineate regions eliciting similar outcome, thus sorting nanomaterials according to their mode-of-action.

6. Conclusion and perspectives

In this work, we show that lung epithelial cells respond to a specific particulate exposure by excreting internalized nanomaterials and passivating them on their surface, employing lipid-wrapping mediated inactivation of nanoparticles through elevated lipid synthesis. Macrophages, however, inevitably attack the stressed and defending epithelium but die while degrading the passivized bio-nano agglomerates. Consequently, the nanomaterial is released into the intercellular space and becomes available for re-uptake by the epithelial cells, closing the first loop. The continuing proinflammatory signalling recruits new phagocytes that feed this vicious cycle of events, resulting in a long-lasting response to a single exposure to nanomaterial.

The unraveled pathway allowed us to build a mechanistic model for prediction of long-term *in vivo* chronic inflammation with the use of only *in vitro* measurements and *in silico* modeling. Based on this success, we contend that the game-changing screening strategy in nanotoxicology should be based on a detailed understanding of the response of the organism to nanomaterial exposure from the initial contact with the nanomaterial to the potential adverse outcome. Although this way requires the use of advanced imaging, omics, particle labelling and tracking techniques at the stage of analysis of *in vivo* and *in vitro* data, it enables the development of novel cost-efficient high-throughput alternative-to-animal testing strategies. The nonlinear initiation of adverse outcome pathways, such as the cycle of events presented here fueling the nanomaterial-induced chronic inflammation, could inspire future research towards a mechanistic understanding of endless adverse cycles in cancer, fibrosis, and other chronic diseases.

Methods

This is a condensed description of the methods. Details are available in the Supplementary Information in the general section "S0a – general materials and methods" for general methods as well as for each experiment separately.

Materials

Alexa Fluor 647 NHS ester (Termo Fisher), Star 520 SXP NHS ester (Abberior), ATTO 594 NHS ester (Atto-tec), CellMask Orange (Invitrogen), SiR Actin (Cytoskeleton), Star Red-DPPE (Abberior), 4-(8,9-Dimethyl-6,8-dinonyl-2-oxo-8,9-dihydro-2H-pyrano[3,2-g]quinolin-3-yl)-1-(3-

(trimethylammonio) propyl)pyridin-1-ium dibromide(SHE-2N), 3-(Benzo[d]thiazol-2-yl)-6,8,8,9-tetramethyl-2-oxo-8,9-dihydro-2H-pyrano[3,2-g]quinoline-4-carbonitrile (SAG-38), LCIS-Live Cell Imaging Solution (Invitrogen), PBS-phosphate buffer saline (Gibco), 100x dcb: 100-times diluted bicarbonate buffer (pH 10, osmolarity 5 miliosmolar, mixed in-house), F-12K cell culture medium (Gibco), RPMI 1640 cell culture medium (Gibco), Trypsin (Sigma), Penicillin-Streptomycin (Sigma), Non-essential amino acids (Gibco), Beta mercaptoethanol (Gibco), glucose (Kemika), BSA-bovine serum albumin (Sigma), Hydrogen peroxide (Merck), Chlorpromazine (Alfa Aesar), MBCD-Metyl-Beta-Cyclodextran (Acros organics), Resveratrol (Sigma), #1.5H μ-dishes (Ibidi,) #1.5H μ-Slide 8-well (Ibidi), Limulus Amebocyte Lysate Assay (Lonza, Walkersville, MD, USA), 10% neutral buffered formalin (CellPath Ltd, UK), haematoxylin and eosin (H&E), Pelcotec™ SFG12 Finder Grid Substrate- Si wafers (Ted Pella), Aeroneb®Pro nebulizer (from VITROCELL® Cloud 6 system), GeneChip® WT PLUS Reagent Kit (Thermo Fisher/Affymetrix), RNeasy Plus Mini Kit (Qiagen), WT PLUS Reagent Kit (Thermo Fisher Scientific Inc., Waltham, USA), Mouse Clariom S arrays (Thermo Fisher Scientific)

Nanomaterials used in this study

Synthesized in-house by P. Umek:

TiO$_2$ nanotubes (PU–nTOX–01–03) and TiO$_2$ nanocubes (PU–nTOX–01–21);

Kind gift from U. Vogel:

carbon black (Printex 90), TiO$_2$ MKNA015 (MKN- TiO$_2$ -A015), TiO$_2$ MKNA100 (MKN- TiO$_2$ -A100) and quartz silica (SiO$_2$ DQ12);

Kind gift from JRC Nanomaterial Repository:

NM-101 TiO2 anatase (TiO2-NM101-JRCNM01001a), NM-105 TiO2 rutil-anatase (TiO2-NM105-JRCNM01005a), NM-110 ZnO (ZnO-NM110-JRCNM62101a), and NM 111 ZnO (ZnO-NM111-JRCNM01101a), NM-200 SiO2 (SiO2-NM200-JRCNM02000a), NM-401 MWCNT (MWCNTs-NM401-JRCNM04001a), NM-402 MWCNT (MWCNTs-NM402-JRCNM04002a).

Software

Imspector (version 16.2.8282-metadata-win64-BASE) software provided by Abberior

SPCImage 7.3 (Becker & Hickl)

Fiji, ImageJ 1.52p (NIH)

syGlass (http://www.syglass.io/, RRID:SCR_017961)

Mathematica 12.0, licence L5063-5112 (Wolfram)

genomics software: GSEA by Broad Institute

modelling: GROMACS 2018.3 (calculation), VMD (visualisation)

TiO_2 nanotubes synthesis and labelling

The TiO_2 anatase nanotubes used in this paper were synthesized, functionalized with AEAPMS, and labelled with STED-compatible fluorescent probes via a covalent reaction between the AEAPMS and ester functional group on the probe. All this was done in-house as described in reference [27]. Labelled TiO_2 was then stored suspended in 100x diluted bicarbonate buffer. For the multi-nanomaterial exposure experiments we used other NMs as well. In this case, the nanomaterials were suspended in PBS and sonicated in ice bath using a tip sonicator (Sonicator 4000, Misonix, with 419 Microtip probe) for 15 min with 5s ON/ 5s OFF steps.

Cell culture

Murine epithelial lung tissue cell line (LA- 4; cat. no. ATCC CCL-196) and murine alveolar lung macrophage (MH-S; cat. No. CRL2019) cell line were purchased from and cultured according to American Type Culture Collection (ATCC) instructions. Cells were cultured in TPP cell culture flasks at 37 °C in a 5% CO_2 humidified atmosphere until monolayers reached desired confluency. All experiments were performed with cells before the twentieth passage. For long–term live cell experiments we used a homemade stage-top incubator which maintains a humidified atmosphere with a 5% CO_2 and is heated to 37 °C.

Medium used for culturing of the epithelial LA-4 cells is Ham's F-12K medium (Gibco) supplemented with 15% FCS (ATCC), 1% P/S (Sigma), 1% NEAA (Gibco), 2 mM L-gln.

For alveolar macrophages, MH-S, cell line we used RPMI 1640 (Gibco) medium supplemented with 10% FCS (ATCC), 1% P/S (Sigma), 2 mM L-gln, and 0.05 mM beta mercapthoethanol (Gibco).

In vitro sample preparation and exposure

LA-4 and MH-S cells were seeded in Ibidi 1.5H dishes of various surface area, depending on the experiment. After 24 h, nanomaterial (c=1mg/mL) was added at an appropriate surface dose $(S_{NP}:S_{cells})$, according to the experiment needs. Before exposure, nanomaterial suspension was sonicated for 10 s in an ultrasonic bath (Bransonic ultrasonic cleaner, Branson 2510EMT). Cells were then incubated at 37 °C and 5% CO_2 atmosphere with the nanomaterial for the desired time in order to observe the cells at the post-exposure time points of interest. If the experiment required monoculture of either cell line, sample were prepared as described above, if however, we experimented with the co-cultures, sample preparation differed slightly. For co-cultures, we grew LA-4 and MH-S in separate dishes up to desired confluency (lower than for monocultures) and then mixed them together by adding MH-S in the LA-4 dish at a ratio of 1 : 40. Co-cultures were then incubated for 24 h more, exposed to nanomaterial as described above and incubated for additional desired amount of time. Growth medium for co-cultures was mixture of equal volumes of F12K and RPMI 1640. Cells were then labelled with fluorescent dyes according to the manufacturer's recommendations. Right before observing the live cells, unbound fluorescent label was washed and medium was exchanged for LCIS.

In some experiments we used different chemicals for modulation of the cell metabolism. For blocking the Clathrin-mediated endocytosis, cells were treated with 100 µm Chlorpromazine for 15 min. Membrane cholesterol was extracted with a 24 h incubation with 0.5 - 1 mM MBCD. FAS was inhibited with overnight 100 µM Resveratrol incubation. Finally, for actin stabilization, we used higher concentration ($\geq$1mM) of Sir-Actin Label based on Jasplankinolide. All the chemical modulators were added before exposure to nanomaterial and continued to be incubated with the cells even after during incubation with the nanomaterial for abovementioned time periods.

For the reuptake experiments different cell lines were grown separately, and washed with PBS before adding MH-S to LA-4.

HIM, SEM

Samples were prepared as usual but we grew them on Si-wafers. After reaching desired confluency samples were freeze-dried with metal mirror freezing technique.

Imaging *in vitro*

STED

Super-resolution and confocal fluorescence micrographs were acquired using custom build STED microscope from Abberior with an Olympus IX83 microscope and two avalanche photodiodes as detectors (APDs). The microscope is equipped with two 120 picosecond pulsed laser sources (Abberior) with excitation wavelengths 561 and 640 nm and maximal power of 50 µW in the sample plane. Pulse repetition frequency for experiments was 40 - 80 MHz, depending on the experiment. STED depletion laser wavelength is 775 nm with same repetition frequency as excitation lasers, pulse length of 1.2 ns and maximal power of 170 mW in the sample plane. Filter sets used for detection were either 605–625 nm (green channel) or 650–720 nm (red channel). Images were acquired using Imspector (version 16.2.8282-metadata-win64-BASE) software also provided by Abberior. All microscope settings were tuned separately for maximal resolution during each of the experiments and are listed with alongside the recorded images in Supplementary Information.

FLIM

Fluorescence lifetime images (FLIM) were obtained on the same custom-built STED microscope (Abberior instruments) as confocal and STED fluorescence images in this study. This time, the emitted fluorescence was detected using PMT detectors and TCSPC technology developed by Becker & Hickl. 16-channel GaASP PMT detectors attached to a spectrograph with diffraction grating 600 l/mm were used to measure fluorescence lifetime of emitted photons with wavelengths ranging from 560 to 760 nm. Spectral information was discarded and the lifetimes were gathered in Imspector 16.2 (Abberior Instruments).

The fluorescence lifetime data was analysed with SPCImage 7.3 software (Becker & Hickl), where the Decay matrix was calculated from the brightest pixel in the image (monoexponential fitting), binning was set to 3 and threshold to 5. The rainbow LUT was rescaled to range from 500 ps to 1000 ps for all images and both intensity and contrast of the lifetime-coded image were adjusted for easier comparison of lifetimes between samples.

Imaging of nanomaterial in backscatter mode:

In Figure 1c, simultaneously with measuring fluorescence from CellMask Orange in the cell membrane (as described in STED section), backscattered light was detected as well to locate the nanomaterial in the sample. A tuneable Chameleon Discovery laser (Coherent) with 100 fs long pulses, pulse repetition frequency 80 MHz, and maximal average power of 1.7 W at 850 nm was used as the scattering light. The pre-attenuated laser light with a wavelength of 750 nm first passed through a 785 nm built-in dichroic where a fraction of the power was directed onto the sample through the same 60x WI objective (NA 1.2) as the excitation light for fluorescence imaging. The light scattered off the nanomaterial and passed back through the same objective and dichroic, now mostly passing through the dichroic towards the detectors. After passing through a pinhole (0.63 A.U.), the backscattered light was spectrally separated from the fluorescence by a short-pass 725 nm dichroic, afterwards being detected on the same PMT, as described in the FLIM section, this time set to collect light with wavelengths above 725nm.

Due to the large coherence of the laser, the backscattered light exhibited a strong speckle pattern, which was diminished by a 100-nm-wide Gaussian blur on the scattering image, thus decreasing false negative colocalisation of nanomaterial on account of spatial resolution.

SEM

SEM imaging has been performed on MIRA3 Flexible FE-SEM produced by TESCAN, by detection of secondary electrons. Beam powers used have been between 5.0 kV and 15 kV with variable field of view 1.8 μm to 180 μm. All samples have been measured under high pressure vacuum (HiVac). All analysis has been performed in Tescan developed software.

HIM

Super-resolution imaging on the nanoscale was carried out using Helium Ion Microscope (Orion NanoFab, Zeiss) available at IBC at the Helmholtz-Zentrum Dresden - Rossendorf e. V., a member of the Helmholtz Association. Microscope equipped with GFIS injection system and additional in-situ backscatter spectrometry and secondary ion mass spectrometry can achieve 0.5 nm lateral resolution imaging using 10-35 keV He ion beams. Measurements of secondary electrons (Se) emitted from the first few nm of the sample were done by He ion acceleration of 30 keV, current of 1.7 pA and were acquired under high vacuum inside the sample chamber (3x10-7 mBar). Field-of-view was varied from

60 µm x 60 µm down to 1 µm x 1 µm, with pixel steps small as 2nm. Imaging was performed on non-tilted and tilted sample stage (45 degrees) for better 3-D visualization.

TEM

ZnO and coated ZnO: Of each material 1 mg was dispersed in 1 mL MilliQ water, except CNTs in 1 mL tannic acid solution 300mg/L, using a vial tweeter for 15 min. Each suspension was diluted 1/10 and 3 µL drop deposited on Formvar Carbon coated 200 mesh copper grids (Agar Scientific, USA) and dehydrated overnight in a desiccator before analysis. Images were collected by JEOL JEM-2100 HR-transmission electron microscope at 120kV (JEOL, Italy) at JRC[40].

TiO$_2$ nanotubes: The nanoparticles were dispersed in water and the dispersion sonicated in water bath for ~3h before use. Of each sample 5 µl was deposed onto glow-discharged copper grid (Agar scientific Ltd, UK) for one minute and the excess of sample was removed blotting with filter paper. After shortly washing with one drop of water, the grid was therefore immersed into a 2% uranyl acetate (UA) solution for 20 s and blotted again with filter paper. The grids were imaged using a JEOL JEM-2100F fitted with a Gatan Orius SC 1000 camera (2x4k).

Transcriptomics *in vitro*

Cells were grown in 6-well plates and exposed to TiO$_2$ nanotubes for 4 h and 48 h, control samples were taken at 0 h and 48 h. Samples were prepared as described above. Briefly, growth medium was removed and the 6-well plates containing cells only were frozen at -70°C. Total RNA was isolated employing the RNeasy Plus Mini Kit (Qiagen). The Agilent 2100 Bioanalyzer was used to assess RNA quality and RNA with RIN>7 was used for microarray analysis.

Total RNA (120 ng) was amplified using the WT PLUS Reagent Kit (Thermo Fisher Scientific Inc., Waltham, USA). Amplified cDNA was hybridized on Mouse Clariom S arrays (Thermo Fisher Scientific). Staining and scanning (GeneChip Scanner 3000 7G) was done according to manufacturer`s instructions.

Statistical analysis for all probe sets included limma t-test and Benjamini-Hochberg multiple testing correction. Raw p-values of the limma t-test were used to define sets of regulated genes (p<0.01). Detection Above Background (dabg) p-values were used to exclude background signals: significant

genes were filtered for p<0.05 in more than half of the samples in at least one group. Array data has been submitted to the GEO database at NCBI (GSE146036).

In the arrow graphs, only genes which were up- or down-regulated more than two times compared to non-exposed cells are shown. The signal (x axis) is drawn in logarithmic scale. Expression is normalized to expression of control samples.

In vivo data

Preparation and characterization of TiO_2 nanotube suspensions

TiO_2 nanotubes were suspended in nanopure water with 2 % v/v mouse serum (prepared in-house) to a final concentration of 3.24 mg/ml. The suspension was probe sonicated on ice for 16 min with 10 % amplitude. 3.24 mg/ml corresponds to a dose of 162 µg TiO_2 nanotubes per 50 µl instillation volume per mice. The vehicle of nanopure water with 2 % v/v mouse serum was probe sonicated using the same protocol. The dose of 162 µg/mouse corresponds to an average surface dose of 3:1 $S_{nanomaterials}$:S_{cells} and is equivalent to 15 working days at the 8-h time-weighted average occupational exposure limit for TiO_2 by Danish Regulations (6.0 mg/m^3 TiO_2).

The average hydrodynamic particle size of the TiO_2 nanotube in suspension (3.24 mg/ ml) was determined by Dynamic Light Scattering (DLS). The TiO_2 nanotube suspension had a bimodal size distribution with a major peak at 60 nm and a narrow peak at 21 nm [13] .The intensity-based zaverage size was 168.7 nm and the polydispersity index (PI) was 0.586, indicating some polydispersity in the suspensions. Endotoxin levels were measured using the Limulus Amebocyte Lysate Assay. The level of endotoxins was low in TiO_2 tube suspensions (0.095 endotoxin units (EU)/mL), and in nanopure water with 2 % mouse serum (0.112 EU/ml).

Animal handling and exposure

Seven-week-old female C57BL/6jBomtac mice (Taconic, Ejby, Denmark) were randomized in groups for TiO_2 nanotube exposure (N=5 mice/group for histology) and vehicle controls (N = 2-4 mice/group). At 8 weeks of age the mice were anaesthetized and exposed to 0 µg or 162 µg TiO_2 nanotube in 50 µl vehicle by single intratracheal instillation. In brief, the mice were intubated in the trachea using a

catheter. The 50 µl suspension was instilled followed by 200 µL air. The mouse was transferred to a vertical hanging position with the head up. This ensures that the administered material is maintained in the lung. Animal experiments were performed according to EC Directive 2010/63/UE in compliance with the handling guidelines established by the Danish government and permits from the Experimental Animal Inspectorate (no. 2015-15-0201-00465). Prior to the study, the experimental protocols were approved by the local Animal Ethics Council.

More details regarding the animal study can be found in Danielsen et al. [13].

Histology and enhanced darkfield imaging

At 28, 90 or 180 days post-exposure mice were weighed and anesthetized. Lungs were filled slowly with 4% formalin under 30 cm water column pressure. A knot was made on the trachea to secure formaldehyde in lungs to fixate tissue in "inflated state". Lungs were then removed and placed in 4% neutral buffered formaldehyde for 24 hours. After fixation the samples were trimmed, dehydrated and embedded in paraffin. 3 µm thin sections were cut and stained with haematoxylin and eosin (H&E). Cytoviva enhanced darkfield hyperspectral system (Auburn, AL, USA) was used to image particles and organic debris in the histological sections of mouse lungs. Enhanced darkfield images were acquired at 100x on an Olympus BX 43 microscope with a Qimaging Retiga4000R camera.

Transcriptomics *in vivo*

Microarray mRNA analysis was performed using Agilent 8×60 K oligonucleotide microarrays (Agilent Technologies Inc., Mississauga, ON, Canada) as described previously [41] with six replicas for each condition. Bioinformatics analysis of the row data: signal intensities were Loess normalized using the limma package in R/Bioconductor [42]. Analysis of differentially expressed genes (DEGs) was performed using the limma package. The genes were considered as significantly differentially expressed if the BH-adjusted p-values were less than or equal to 0.1. Statistical analysis is same as for the *in vitro* transcriptomics above.

Comparison of transcriptomics *in vitro* and *in vivo*

Mice were exposed to 18, 54 or 162 µg of TiO_2 nanotubes per mouse and lungs were harvested on 1st and 28th day post exposure for transcriptomic analysis to evaluate overlapping sets of genes differentially expressed in the *in vivo* and *in vitro* experimental data. The goal of the analysis is to determine and compare alterations in lipid metabolism, immune response in terms of proinflammatory

signalling and cholesterol metabolism between two experimental systems. For the assessment of the monocyte influx, all genes encoding monocyte chemoattractive (C-C motif) chemokines were selected and their expression evaluated.

Modelling

Atomistic molecular dynamics simulation

System composition

Atomistic molecular dynamics simulations have been carried out for DMPC and POPE lipids near anatase (101) TiO_2 surface in water environment. Anatase slab (71.8 x 68.2 x 30.5 Å) with (101) surface normal to the z axis is used as a model of a nanoparticle surface. The slab contains 4536 Ti atoms of which 504 are five-fold coordinated atoms on the surface. (101) anatase surface was chosen as a surface of the lowest energy. At neutral pH TiO_2 surface is covered by hydroxyl groups and is negatively charged. In our model we bind hydroxyl groups to 5-coordinated surface Ti atoms so that the surface charge density is close to the experimental value at neutral pH. Thus we add 151 hydroxyl groups to randomly picked Ti surface atoms (which constitutes 30% of their total amount) which results in a surface charge density of -0.62 electrons/nm^2, which is in line with the experimental results[43].

The TiO_2 slab is then placed in the middle of the simulation box with 3D periodic boundary conditions. The box size in X and Y directions is defined by the slab length and width so that the slab is periodic in those directions. The height of the box is set to 130 Å to accommodate the TiO_2 slab (thickness of 30.5 Å), eventual formed lipid bilayer on the both sides (2 x 40 Å) as well as their hydration layers (2 x 10 Å). 82 lipid molecules (POPE or DMPC) are inserted at random unoccupied positions in the box in random orientations, after that the box is filled with water molecules (about 12000). Then, a small number of water molecules are picked at random and are substituted with Na^+ and Cl^- ions to balance the negative surface charge of the slab and provide NaCl concentration of 0.15 M in the water phase of the simulated system.

Simulation protocol

First, energy minimization of the simulated systems using the steepest gradient descent method is performed, followed by a short 100 ps pre-equilibration run at constant volume and temperature. After that, the pressure in the system is equilibrated to 1 bar using anisotropic Berendsen barostat[44] with relaxation time of 5 ps during 10 ns, which is finally followed by 1 µs production run in the NVT

ensemble. Leap-frog algorithm with time step 1 fs is used to integrate the equations of motion. Center-of-mass motion is removed every 100 steps. Verlet cut-off scheme[45] with the buffer tolerance of 0.005 kJ x mol^{-1} x ps^{-1} per atom is used to generate the pair lists. Minimum cut-off of 1.4 nm is used for both short ranged electrostatic and VdW interactions. Long range electrostatics are calculated using PME[46] with the grid spacing of 0.12 nm and cubic interpolation. Long range dispersion corrections are applied to both energy and pressure. Velocity rescaling thermostat[47] is used to control the temperature, which is set to 303 K with the relaxation time of 1 ps. All bonds with hydrogen atoms are constrained using the LINCS algorithm[48]. Atom coordinates and energies are saved every 5 ps. All simulations were performed by the Gromacs 2019 software package[49]. Visualization of the simulations is done by VMD[50].

Models used

Lipids are described by the Slipids force field[51]. For TiO_2, we use parameters optimized to fit results on charge density distributions and water-TiO_2 surface coordination obtained in *ab-initio* simulations of TiO_2-water interface[52]. These parameters are listed in tables in SI section S2e. Water molecules are represented by the TIP3P model[53], and for Na^+ and Cl^- ions Yoo and Aksimentiev ion parameters is used[54]. Lorentz-Berthelot rules are applied to determine Lennard-Jones parameters for cross-interactions.

Model of chronic inflammation following nanomaterial exposure

The theoretical model of chronic inflammation following nanomaterial exposure is described by a series of differential equations (see S5b), describing the events observed in *in vitro* and *in vivo* experiments in this work. This minimal-complexity *in vivo* model consists of 6 variables (surface of nanomaterial in epithelial cells, in cauliflowers, in macrophages and freely-floating nanomaterial, surface of macrophages and surface of epithelial cells), 4 fixed parameters which are calibrated for each model system and later locked (endocytosis rate, rate of cauliflower endocytosis, delay between cauliflower production and signalling for macrophage influx, and epithelial cell replication rate) and 3 NM-associated parameters (cauliflower formation rate *cff*, signalling efficiency *signEff*, and toxicity *tox*). Separate *in vitro* models were obtained from the *in vivo* model by swapping the macrophage influx with macrophage replication and leaving out non-existent cells for monocultures.

The system of equations was solved numerically using Wolfram Mathematica 12.0, licence L5063-5112 to obtain the time evolution and final state of the model. The same software was also used for visualization of the results.

The phase space was scanned by calculating the time evolution of the appropriate system of equations from chapter S5b for a set of nanomaterials with appropriately interspaced parameters: toxicity (*tox*), cauliflower formation (*cff*) and signalling efficiency (*signalEff*). For each parameter, 30 logarithmically-equally-spaced values in a sensible range were chosen – the total amount of values in the grid was thus 30 x 30 x 30 = 27.000.

More information can be found in Supplementary Information.

Data availability

Source data is publically available online at http://lbfnanobiodatabase.ijs.si/file/data/cauliflowerpaper/ with all 3Ds,movies and raw tiffs as a part of a database develop for H2020 Smart Nano Tox project.

Source data for *in vitro* genomics was deposited in the GEO database under the number GSE146036 and is accessible via the link https://www.ncbi.nlm.nih.gov/geo/query/acc.cgi?acc=GSE146036 using the token listed in the attached Reporting Summary, section "Data".

References

1. Netea, M. G. *et al.* A guiding map for inflammation. *Nat. Immunol.* **18**, 826–831 (2017).
2. Furman, D. *et al.* Chronic inflammation in the etiology of disease across the life span. *Nat. Med.* **25**, 1822–1832 (2019).
3. Roth, G. A. *et al.* Global, regional, and national age-sex-specific mortality for 282 causes of death in 195 countries and territories, 1980–2017: a systematic analysis for the Global Burden of Disease Study 2017. *The Lancet* **392**, 1736–1788 (2018).
4. Underwood, E. The polluted brain. *Science* **355**, 342–345 (2017).

5. OECD. OECD Environmental Outlook to 2050. doi:http://dx.doi.org/10.1787/9789264122246-en.

6. WHO. Air pollution. https://www.who.int/westernpacific/health-topics/air-pollution.

7. EPA/600/R-12/056F Provisional Assessment of Recent Studies on Health Effects of Particulate Matter Exposure. (2012).

8. Rohr, J. R., Salice, C. J. & Nisbet, R. M. Chemical safety must extend to ecosystems. *Science* **356**, 917–917 (2017).

9. Huh, D. *et al.* Reconstituting Organ-Level Lung Functions on a Chip. *Science* **328**, 1662–1668 (2010).

10. Forest, V., Hochepied, J.-F. & Pourchez, J. Importance of Choosing Relevant Biological End Points To Predict Nanoparticle Toxicity with Computational Approaches for Human Health Risk Assessment. *Chem. Res. Toxicol.* **32**, 1320–1326 (2019).

11. Maynard, A. D. & Aitken, R. J. 'Safe handling of nanotechnology' ten years on. *Nat. Nanotechnol.* **11**, 998–1000 (2016).

12. Nel, A. E. & Malloy, T. F. Policy reforms to update chemical safety testing. *Science* **355**, 1016–1018 (2017).

13. Danielsen, P. H. *et al.* Effects of physicochemical properties of TiO2 nanomaterials for pulmonary inflammation, acute phase response and alveolar proteinosis in intratracheally exposed mice. *Toxicol. Appl. Pharmacol.* **386**, 114830 (2020).

14. Fujita, K. *et al.* Intratracheal instillation of single-wall carbon nanotubes in the rat lung induces time-dependent changes in gene expression. *Nanotoxicology* **9**, 290–301 (2015).

15. Cho, W.-S. *et al.* NiO and Co3O4 nanoparticles induce lung DTH-like responses and alveolar lipoproteinosis. *Eur. Respir. J.* **39**, 546–557 (2012).

16. van den Brule, S. *et al.* Nanometer-long Ge-imogolite nanotubes cause sustained lung inflammation and fibrosis in rats. *Part. Fibre Toxicol.* **11**, 67 (2014).

17. Tian, F. *et al.* Pulmonary DWCNT exposure causes sustained local and low-level systemic inflammatory changes in mice. *Eur. J. Pharm. Biopharm.* **84**, 412–420 (2013).

18. Kim, S.-H. *et al.* The early onset and persistent worsening pulmonary alveolar proteinosis in rats by indium oxide nanoparticles. *Nanotoxicology* **0**, 1–11 (2019).

19. Kasai, T. *et al.* Lung carcinogenicity of inhaled multi-walled carbon nanotube in rats. *Part. Fibre Toxicol.* **13**, 53 (2016).

20. Kasai, T. *et al.* Thirteen-week study of toxicity of fiber-like multi-walled carbon nanotubes with whole-body inhalation exposure in rats. *Nanotoxicology* **9**, 413–422 (2015).

21. Pauluhn, J. Subchronic 13-week inhalation exposure of rats to multiwalled carbon nanotubes: toxic effects are determined by density of agglomerate structures, not fibrillar structures. *Toxicol. Sci. Off. J. Soc. Toxicol.* **113**, 226–242 (2010).

22. Hotamisligil, G. S. Inflammation and metabolic disorders. *Nature* **444**, 860–867 (2006).

23. Röhrig, F. & Schulze, A. The multifaceted roles of fatty acid synthesis in cancer. *Nat. Rev. Cancer* **16**, 732–749 (2016).

24. Peck, B. & Schulze, A. Lipid Metabolism at the Nexus of Diet and Tumor Microenvironment. *Trends Cancer* **5**, 693–703 (2019).

25. Qiao, Y. *et al.* FABP4 contributes to renal interstitial fibrosis via mediating inflammation and lipid metabolism. *Cell Death Dis.* **10**, 382 (2019).

26. Bourdon, J. A. *et al.* Hepatic and pulmonary toxicogenomic profiles in mice intratracheally instilled with carbon black nanoparticles reveal pulmonary inflammation, acute phase response, and alterations in lipid homeostasis. *Toxicol. Sci. Off. J. Soc. Toxicol.* **127**, 474–484 (2012).

27. Poulsen, S. S. *et al.* Changes in cholesterol homeostasis and acute phase response link pulmonary exposure to multi-walled carbon nanotubes to risk of cardiovascular disease. *Toxicol. Appl. Pharmacol.* **283**, 210–222 (2015).

28. Gaté, L. *et al.* Pulmonary toxicity of two different multi-walled carbon nanotubes in rat: Comparison between intratracheal instillation and inhalation exposure. *Toxicol. Appl. Pharmacol.* **375**, 17–31 (2019).

29. Urbančič, I. *et al.* Nanoparticles Can Wrap Epithelial Cell Membranes and Relocate Them Across the Epithelial Cell Layer. *Nano Lett.* **18**, 5294–5305 (2018).

30. Poulsen, S. S. *et al.* Multi-walled carbon nanotube-physicochemical properties predict the systemic acute phase response following pulmonary exposure in mice. *PLOS ONE* **12**, e0174167 (2017).

31. Saber, A. T. *et al.* Particle-induced pulmonary acute phase response may be the causal link between particle inhalation and cardiovascular disease. *WIREs Nanomedicine Nanobiotechnology* **6**, 517–531 (2014).

32. Pollard, T. D. & Cooper, J. A. Actin, a Central Player in Cell Shape and Movement. *Science* **326**, 1208–1212 (2009).

33. Tran, D. T., Masedunskas, A., Weigert, R. & Hagen, K. G. T. Arp2/3-mediated F-actin formation controls regulated exocytosis in vivo. *Nat. Commun.* **6**, 1–10 (2015).

34. Khaitlina, S. Y. Intracellular transport based on actin polymerization. *Biochem. Biokhimiia* **79**, 917–927 (2014).

35. Li, P., Bademosi, A. T., Luo, J. & Meunier, F. A. Actin Remodeling in Regulated Exocytosis: Toward a Mesoscopic View. *Trends Cell Biol.* **28**, 685–697 (2018).

36. Tran, D. T. & Ten Hagen, K. G. Real-time insights into regulated exocytosis. *J. Cell Sci.* **130**, 1355–1363 (2017).

37. Laskin, D. L., Malaviya, R. & Laskin, J. D. Chapter 32 - Pulmonary Macrophages. in *Comparative Biology of the Normal Lung (Second Edition)* (ed. Parent, R. A.) 629–649 (Academic Press, 2015). doi:10.1016/B978-0-12-404577-4.00032-1.

38. Oberdörster Günter, Oberdörster Eva & Oberdörster Jan. Nanotoxicology: An Emerging Discipline Evolving from Studies of Ultrafine Particles. *Environ. Health Perspect.* **113**, 823–839 (2005).

39. Gosens, I. *et al.* Comparative Hazard Identification by a Single Dose Lung Exposure of Zinc Oxide and Silver Nanomaterials in Mice. *PLoS ONE* **10**, (2015).

40. JRC Nanomaterials Repository. *EU Science Hub - European Commission* https://ec.europa.eu/jrc/en/scientific-tool/jrc-nanomaterials-repository (2014).

41. Søs Poulsen, S. *et al.* Transcriptomic Analysis Reveals Novel Mechanistic Insight into Murine Biological Responses to Multi-Walled Carbon Nanotubes in Lungs and Cultured Lung Epithelial Cells. *PLoS ONE* **8**, (2013).

42. Ritchie, M. E. *et al.* limma powers differential expression analyses for RNA-sequencing and microarray studies. *Nucleic Acids Res.* **43**, e47 (2015).

43. Akratopulu, K. C., Vordonis, L. & Lycourghiotis, A. Effect of temperature on the point of zero charge and surface dissociation constants of aqueous suspensions of γ-Al2O3. *J. Chem. Soc. Faraday Trans. 1 Phys. Chem. Condens. Phases* **82**, 3697–3708 (1986).

44. Berendsen, H. J. C., Postma, J. P. M., van Gunsteren, W. F., DiNola, A. & Haak, J. R. Molecular dynamics with coupling to an external bath. *J. Chem. Phys.* **81**, 3684–3690 (1984).

45. Páll, S. & Hess, B. A flexible algorithm for calculating pair interactions on SIMD architectures. *Comput. Phys. Commun.* **184**, 2641–2650 (2013).

46. Darden, T., York, D. & Pedersen, L. Particle mesh Ewald: An N·log(N) method for Ewald sums in large systems. *J. Chem. Phys.* **98**, 10089–10092 (1993).

47. Bussi, G., Donadio, D. & Parrinello, M. Canonical sampling through velocity rescaling. *J. Chem. Phys.* **126**, 014101 (2007).

48. Hess, B. P-LINCS: A Parallel Linear Constraint Solver for Molecular Simulation. *J. Chem. Theory Comput.* **4**, 116–122 (2008).

49. Abraham, M. J. *et al.* GROMACS: High performance molecular simulations through multi-level parallelism from laptops to supercomputers. *SoftwareX* **1–2**, 19–25 (2015).

50. Humphrey, W., Dalke, A. & Schulten, K. VMD: visual molecular dynamics. *J. Mol. Graph.* **14**, 33–38, 27–28 (1996).

51. Jämbeck, J. P. M. & Lyubartsev, A. P. Derivation and Systematic Validation of a Refined All-Atom Force Field for Phosphatidylcholine Lipids. *J. Phys. Chem. B* **116**, 3164–3179 (2012).

52. Agosta, L., Brandt, E. G. & Lyubartsev, A. P. Diffusion and reaction pathways of water near fully hydrated TiO2 surfaces from ab initio molecular dynamics. *J. Chem. Phys.* **147**, 024704 (2017).

53. Jorgensen, W. L., Chandrasekhar, J., Madura, J. D., Impey, R. W. & Klein, M. L. Comparison of simple potential functions for simulating liquid water. *J. Chem. Phys.* **79**, 926–935 (1983).

54. Yoo, J. & Aksimentiev, A. Improved Parametrization of Li+, Na+, K+, and Mg2+ Ions for All-Atom Molecular Dynamics Simulations of Nucleic Acid Systems. *J. Phys. Chem. Lett.* **3**, 45–50 (2012).

Acknowledgements

Author contributions

These authors have contributed equally: Hana Majaron, Boštjan Kokot, and Aleksandar Sebastijanović as first authors and Tilen Koklič, Tobias Stoeger, and Janez Štrancar as corresponding authors.

Affiliations

Department of Condensed Matter Physics, Jožef Stefan Institute, Ljubljana, Slovenia

Hana Majaron, Boštjan Kokot, Aleksandar Sebastijanović, Rok Podlipec, Patrycja Zawilska, Ana Krišelj, Mojca Pušnik, Petra Čotar, Polona Umek, Stane Pajk, Iztok Urbančič, Tilen Koklič, Janez Štrancar

Jožef Stefan International Postgraduate School, Jamova cesta 39, 1000 Ljubljana, Slovenia

Hana Majaron, Aleksandar Sebastijanović

Faculty of Natural sciences and Mathematics, University of Maribor, Maribor, Slovenia

Boštjan Kokot

Institute of Lung Biology and Disease, Helmholtz Zentrum München, 85764 Neuherberg, Germany

Carola Voss, Carolina Ballester-Lopez, Qiaoxia Zhou, Otmar Schmid, Tobias Stoeger

Ion Beam Center, Helmholz Zentrum Dresden Rossendorf, Dresden, Germany

Rok Podlipec

National Research Centre for the Working Environment, Copenhagen Ø, Denmark

Trine Berthing, Pernille H. Danielsen, Ulla B. Vogel

Department of Chemistry, Molecular Sciences Research Hub, Imperial College London, London, United Kingdom

Claudia Contini, Matthew Schneemilch, Nick Quirke

Department of Materials and Environmental Chemistry, Stockholm University, SE-10691 Stockholm, Sweden

Mikhail Ivanov, Alexander Lyubartsev

Faculty of Mathematics and Physics, University of Ljubljana, Ljubljana, Slovenia

Petra Čotar

Department of Forensic Pathology, Sichuan University, Chengdu, China

Qiaoxia Zhou

European Commission, Joint Research Centre (JRC), Ispra, Italy

Jessica Ponti

School of Medicine, University College Dublin, Belfield, Dublin 4, Ireland

Vadim Zhernovkov

Faculty of Pharmacy, University of Ljubljana, Ljubljana, Slovenia

Mojca Pušnik, Stane Pajk

Institut Jean Lamour, CNRS-Université de Lorraine, Nancy, France

Zahra Manel Doumandji, Olivier Joubert

Institute of Experimental Genetics, Helmholtz Zentrum München, Neuherberg, Germany

Martin Irmler, Johannes Beckers

German Center for Diabetes Research (DZD), Neuherberg, Germany

Johannes Beckers

Chair of Experimental Genetics, Center of Life and Food Sciences, Weihenstephan, Technische Universität München, Freising, Germany

Johannes Beckers

School of Physics, University College Dublin, Belfield, Dublin 4, Ireland

Vladimir Lobaskin

Health Canada, Ottawa, Canada

Sabina Halappanavar

Contributions

HM, BK, AS, CV, RP, PZ, TB, CBL, PHD, CC, VZ, MS, OJ, MIr, JB, VL, SH, NQ, AL, UV, TK, TS, JS designed the study and analysis.

HM, BK, AS, CV, RP, PZ, TB, PHD, CC, AK, PC, QZ, JP, ZMD, MP, PU, SP, MIr, SH prepared the samples.

HM, BK, AS, CV, RP, PZ, TB, PHD, CC, AK, PC, QZ, JP, ZMD, MP, MIr, SH performed the experiments.

HM, BK, AS, CV, RP, PZ, TB, CBL, CC, AK, QZ, JP, VZ, ZMD, MP, MIr, JB, SH, TK, TS, JS analysed the data.

HM, MIv and MS performed the modelling.

OJ, JB, VL, SH, NQ, AL, UV, TK, TS, JS supervised the study.

HM, BK and AS prepared the manuscript with input from all other authors: CV, RP, PZ, TB, CBL, PHD, CC, MIv, AK, PC, QZ, JP, VZ, MS, ZMD, MP, PU, SP, OJ, OS, IU, MIr, JB, VL, SH, NQ, AL, UV, TK, TS, JS.

Corresponding authors

Correspondence to Janez Štrancar, Tobias Stoeger, and Tilen Koklič.

Materials & Correspondence

Materials and correspondence should be addressed to Hana Majaron, Boštjan Kokot or Aleksandar Sebastijanović.

Ethics declarations

Competing interests

The authors declare no competing interests.

Supplementary information

Supplementary information

This file contains the Supplementary Discussion, Supplementary References and a full guide for Supplementary.

Source data

Source Data Fig.1

Source Data Fig.2

Source Data Fig.3

Source Data Fig.4

Source Data Fig.5

Source Data Supplement